

# Numerical analysis of fume formation mechanism in arc welding

Shinichi Tashiro<sup>1,4</sup>, Tasuku Zeniya<sup>1</sup>, Kentaro Yamamoto<sup>1</sup>,  
Manabu Tanaka<sup>1</sup>, Kazuhiro Nakata<sup>1</sup>, Anthony B Murphy<sup>2</sup>,  
Eri Yamamoto<sup>3</sup>, Kei Yamazaki<sup>3</sup> and Keiichi Suzuki<sup>3</sup>

<sup>1</sup> Joining and Welding Research Institute, Osaka University 11-1 Mihogaoka, Ibaraki, Osaka 576-0047, Japan

<sup>2</sup> Materials Science and Engineering, CSIRO, Lindfield, NSW 2070, Sydney, Australia

<sup>3</sup> KOBE STEEL, LTD, 100-1 Miyamae, Fujisawa, Kanagawa 251-8551, Japan

E-mail: [tashiro@jwri.osaka-u.ac.jp](mailto:tashiro@jwri.osaka-u.ac.jp) (S Tashiro)

Received 18 April 2010, in final form 15 June 2010

Published 14 October 2010

Online at [stacks.iop.org/JPhysD/43/434012](http://stacks.iop.org/JPhysD/43/434012)

## Abstract

In order to clarify the fume formation mechanism in arc welding, a quantitative investigation based on the knowledge of interaction among the electrode, arc and weld pool is indispensable. A fume formation model consisting of a heterogeneous condensation model, a homogeneous nucleation model and a coagulation model has been developed and coupled with the GTA or GMA welding model. A series of processes from evaporation of metal vapour to fume formation from the metal vapour was totally investigated by employing this simulation model. The aim of this paper is to visualize the fume formation process and clarify the fume formation mechanism theoretically through a numerical analysis. Furthermore, the reliability of the simulation model was also evaluated through a comparison of the simulation result with the experimental result. As a result, it was found that the size of the secondary particles consisting of small particles with a size of several tens of nanometres reached 300 nm at maximum and the secondary particle was in a U-shaped chain form in helium GTA welding. Furthermore, it was also clarified that most part of the fume was produced in the downstream region of the arc originating from the metal vapour evaporated mainly from the droplet in argon GMA welding. The fume was constituted by particles with a size of several tens of nanometres and had similar characteristics to that of GTA welding. On the other hand, if the metal transfer becomes unstable and the metal vapour near the droplet diffuses directly towards the surroundings of the arc not getting into the plasma flow, the size of the particles reaches several hundred nanometres.

(Some figures in this article are in colour only in the electronic version)

## 1. Introduction

In arc welding, high-temperature metal vapour is generated from the melting tip of a welding wire, a droplet and a weld pool [1]. This metal vapour is cooled rapidly during diffusion to the surroundings of the arc. Then primary particles of metal of size 1–100 nm are formed by nucleation from the metal vapour. Furthermore, some of those particles condense and produce secondary particles with a maximum size of over 1  $\mu\text{m}$ . These particles form a smoke which ascends from the arc and this phenomenon is called fume in welding [2].

Until now, most of the papers show chemical composition and generation rate of the fume in comparison with welding conditions for gas metal arc (GMA) welding because of high utilization at various manufacturing industries in the world. For example, Kobayashi *et al* observed a state of fume generation in shielded metal arc welding by employing a high-speed video camera. It was qualitatively explained that metal vapour which has evaporated mainly from the droplet was released from the lower part of the arc column and generated the fume due to rapid cooling with condensation and oxidation. They also showed that the amount of metal vapour from the droplet was higher than that from the weld

<sup>4</sup> Author to whom any correspondence should be addressed.

pool [2]. Jenkins and Eagar measured chemical composition of fume in shielded metal arc welding and GMA welding by energy dispersive spectrometry (EDS) [3]. Bosworth and Deam discussed the influence of droplet size on fume generation rate in GMA welding [4]. However, studies on the clarification of the theoretical mechanism of fume formation are scarce, because almost all the previous studies were carried out through experimental observations. In order to clarify the fume formation mechanism, it is necessary to discuss the phenomena quantitatively taking account of the interactions among the electrode, the arc and the weld pool. Unfortunately, phenomena in GMA welding are not fully understood due to the complex problem represented by a metal transfer.

On the other hand, the theoretical research approach is advanced in the field of production of industrial nanoparticles. Many researchers reported numerical simulations for clarifying the fume formation mechanism. Watanabe *et al* investigated a series of processes from evaporation of powder by thermal plasma to nucleation and condensation in the cooling region for production of nanoparticles in an inductively coupled plasma (ICP) [5]. However, change in the shape of secondary particles was not considered because all the particles were assumed to be spherical in shape in this model. Schmid *et al* proposed a model considering the change in the shape of secondary particles in a coagulation process, but this model was not coupled with nucleation and condensation processes [6]. From above, it is clear that there have been no studies in which the whole process is totally modelled for clarifying the fume formation mechanism.

The gas tungsten arc (GTA) welding would be namely targeted as the first subject for clarifying the fume formation mechanism because of its simplified problem like a non-metal transfer. Recently, it is actively conducted to analyse the formation mechanism of the weld pool with a numerical simulation treating the electrode, the arc and the weld pool in GTA welding as a total system considering their interactions. Tanaka and Lowke quantitatively showed its formation mechanism using a unified numerical model taking account of thermal and dynamic interactions between the arc and the weld pool [7]. Furthermore, Yamamoto *et al* and Mori *et al* improved this model and additionally discussed the evaporation of the metal vapour from the weld pool and its diffusion in the arc [8,9]. However, the fume formation mechanism from the metal vapour has not been reported in arc welding.

This paper aims to clarify the fume formation mechanism theoretically through a visualization of the fume shape. In this paper, a series of processes such as evaporation of metal vapour due to the arc and the formation of fume from the metal vapour is totally discussed by a numerical simulation which is calculated by coupling a GTA welding model with a fume formation model. Furthermore, a GMA welding model which takes account of metal transfer is developed based on the GTA welding model, and then, the general mechanism of fume formation for the arc welding process is discussed.

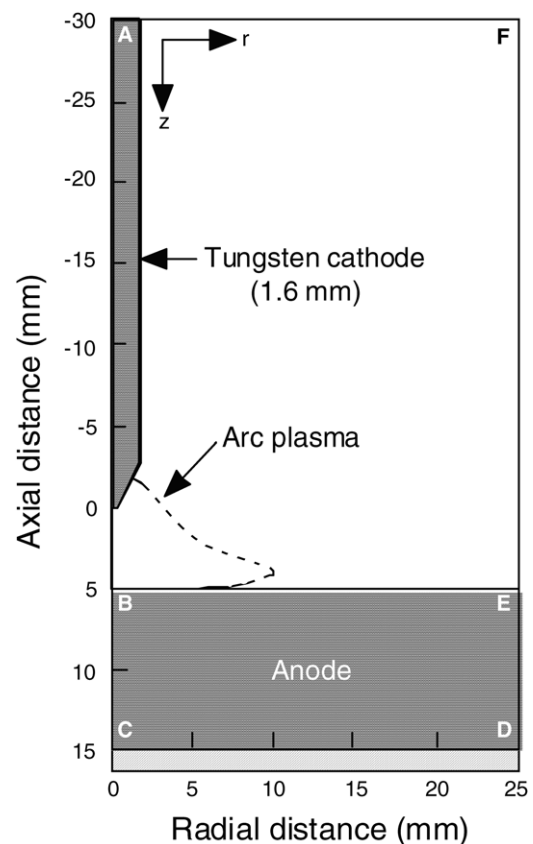


**Figure 1.** Schematic illustration of simulation domain for GTA welding.

## 2. Simulation model

The simulation model employed in this study consists of a GTA welding model [8] and a fume formation model. Additionally, a GMA welding model taking account of metal transfer process has also been developed for coupling that with the fume formation model. The metal vapour pressure and the cooling rate at a nucleation site are calculated by applying a welding condition to the GTA welding model or the GMA welding model. Then, the formation of primary particles and secondary particles is studied by assuming metal vapour pressure and cooling rate as the calculation condition and the mechanism of fume formation is discussed. Details of the simulation models are introduced as follows.

### 2.1. GTA welding model

This model is concerned with the stationary GTA welding using a tungsten cathode of 3.2 mm diameter with a 60° conical tip. Figure 1 shows the simulation region described in the two-dimensional cylindrical coordinates assuming rotational symmetry around the arc axis. The anode material is pure iron. Helium gas is selected as the shielding gas because of the large amount of metal vapour and smut which are generated in the welding process [10]. The shielding gas is supplied from the outer side of the cathode on the upper boundary at a flow rate of 30 Lmin<sup>-1</sup>. An arc current of dc 200 A is applied inside the tungsten cathode on the top boundary and the potential of

the bottom boundary is set to be 0 V. A steady state is assumed. The governing equations consist of conservation equations of mass, momentum, energy and current. The governing equations and the boundary conditions used in this simulation are the same as those in [10].

A mass conservation equation is applied to take metal vapour behaviour into account as expressed in equation (1) [11]. Only iron vapour is taken into account because the anode employed in this study is made of pure iron.

$$\begin{aligned} \frac{\partial}{\partial t}(\rho C_1) + \frac{1}{r} \frac{\partial}{\partial r}(r\rho v_r C_1) + \frac{\partial}{\partial z}(\rho v_z C_1) \\ = \frac{1}{r} \frac{\partial}{\partial r} \left( r\rho D \frac{\partial C_1}{\partial r} \right) + \frac{\partial}{\partial z} \left( \rho D \frac{\partial C_1}{\partial z} \right), \end{aligned} \quad (1)$$

where  $\rho$  is the mass density,  $v$  is the flow velocity,  $C_1$  is the mass fraction concentration of metal vapour and  $D$  is the diffusion coefficient which is expressed by the viscosity approximation equation [12]:

$$D = \frac{2\sqrt{2}(1/M_1 + 1/M_2)^{0.5}}{[(\rho_1^2/\beta_1^2\eta_1^2M_1)^{0.25} + (\rho_2^2/\beta_2^2\eta_2^2M_2)^{0.25}]^2}, \quad (2)$$

where  $M_1$  and  $M_2$  are the molecular weights of iron and the shielding gas, respectively.  $\rho_1$ ,  $\rho_2$  and  $\eta_1$ ,  $\eta_2$  are the density and viscosity of iron and the shielding gas, respectively.  $\beta_1$  and  $\beta_2$  are dimensionless constants defined as  $\beta_i = (D_{ii}\rho_i)/\eta_i$  and range between 1.2 and 1.543 theoretically for various kinds of gases such as Ar, He, H<sub>2</sub>, N<sub>2</sub>, O<sub>2</sub> and CO<sub>2</sub>.  $\beta_1 = \beta_2 = 1.385$  is assumed based on the mean value of the experimental data [12]. The viscosity approximation is acceptable up to 30 000 K [13] because viscosity which is calculated as a plasma property takes ionized matter into account, and hence it is considered to be suitable for modelling welding arcs.

On the anode surface (BE) where the temperature is above the melting point,  $C_1$  is given as [11]

$$C_1 = \frac{p_{v,1}M_1}{p_{v,1}M_1 + (p_{\text{atm}} - p_{v,1})M_2}, \quad (3)$$

where  $p_{\text{atm}}$  is the atmospheric pressure and  $p_{v,1}$  is the partial pressure of the metal vapour which is a function of the weld pool temperature [14]. According to the above equation,  $C_1$  varies between zero and 1.0. For the other boundary conditions,  $C_1 = 0$  at AF and FE shown in figure 1, and  $(\partial C_1/\partial r) = 0$  at the arc axis (AB).

In the present model, the plasma properties are dependent on not only the temperature but also the mole fraction of the metal vapour. The plasma properties at intermediate concentrations of metal vapour are calculated using a linear approximation based on the properties at 0, 1, 10, 20 and 30 mol% of metal vapour mixture rate [15]. The properties were calculated using the Chapman–Enskog approximation [15] under the assumption that the arc plasma is in a local thermodynamic equilibrium (LTE) state. All of electron temperature, ion temperature and heavy particle temperature are the same under the LTE condition. The governing and auxiliary equations were solved iteratively by the SIMPLEX numerical procedure [16].

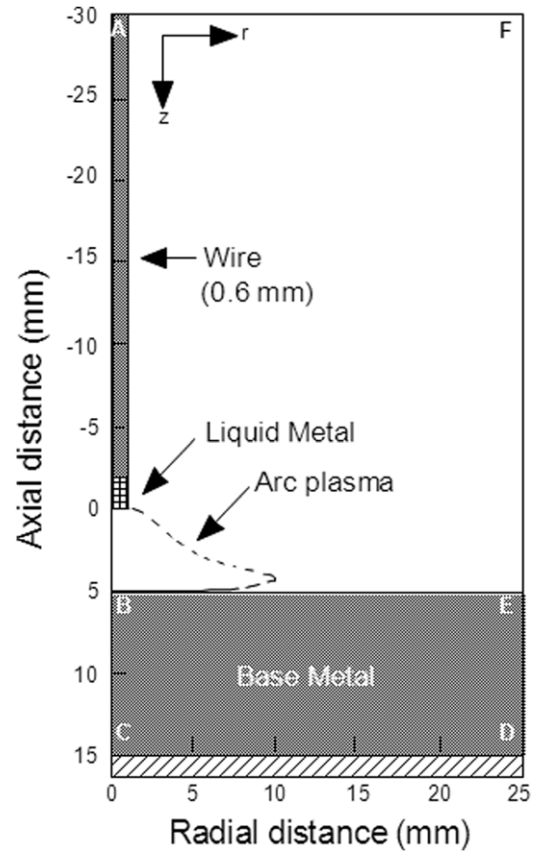


**Figure 2.** Schematic illustration of simulation domain for GMA welding.

## 2.2. GMA welding model

The GMA welding model taking account of the metal transfer process has been developed for coupling that with the fume formation model. Figure 2 shows a simulation region consisting of an electrode wire, an arc and a base metal. The diameter of the electrode wire is 1.2 mm and the thickness of the base metal is 10 mm. The electrode wire and the base metal are pure iron. The arc length is 5 mm with dc electrode positive (dcEP) polarity. An arc current of dc 200 A is applied inside the electrode wire on the top boundary and the potential of the bottom boundary is set to be 0 V. Argon gas is introduced as the shielding gas from the top boundary at a flow rate of 10 Lmin<sup>-1</sup>. The length of the electrode wire is 30 mm in the initial state. It is assumed that the electrode wire above the position at a distance of 29.4 mm from the top boundary is always in the solid phase and that below this position is in the liquid phase. The droplet can be formed at the tip of the electrode wire with a balance among its surface tension, gravity and electromagnetic pinch force, and then can also be detached from the tip of the electrode wire to the base metal, which is called metal transfer. In the calculation of the droplet temperature, energy loss due to the latent heat for evaporation of the metal vapour was taken into account. The volume of fluid (VOF) method is used for the calculations of formation, detachment and transfer of the droplet. The region of the electrode wire is assumed to be initialized after the metal transfer immediately. In this model, time-dependent calculation is conducted for treating the metal

transfer dynamically and ended at a time corresponding to the duration of 2 cycles of metal transfer. The other calculation methods are the same as those of GTA welding model.

### 2.3. Fume formation model

A simulation model for discussing the fume formation mechanism has been developed. In this model, the following assumptions are employed.

- (1) The supersaturation of the iron vapour by cooling.
- (2) The formation of primary particles by homogeneous nucleation.
- (3) The growth of primary particles by heterogeneous condensation.
- (4) The formation of secondary particles by coagulation.
- (5) The growth of secondary particles by heterogeneous condensation and coagulation.

#### 2.3.1. Homogeneous nucleation model of primary particle.

In this paper, Friendlander's liquid-drop model, in which all the nuclei are assumed to be generated in the liquid phase, is employed [17]. In theory, homogeneous nucleation can arise if the degree of supersaturation exceeds 1. It is assumed that a nucleus with a critical diameter  $d_{\text{peri}}$  is generated due to nucleation. The critical diameter is the smallest nucleus's diameter and a nucleus can be stable if its diameter is larger than the critical diameter which is represented by

$$d_{\text{peri}} = \frac{4\sigma_p v_m}{kT \ln S}, \quad (4)$$

where  $\sigma_p$  is the surface tension,  $v_m$  is the volume of the iron atom,  $k$  is the Boltzmann constant,  $T$  is the temperature and  $S$  is the degree of supersaturation. The homogeneous nucleation rate  $J$  which is the number of nuclei generated per unit volume and unit time is written as [18]

$$J = N \frac{\zeta n_1}{12} \sqrt{\frac{\Theta}{2\pi}} \exp\left[-\frac{4\Theta^3}{27(\ln S)^2}\right], \quad (5)$$

where  $N$  is a normalization constant given by equation (6). The Brownian collision between iron atoms  $\zeta$  is represented by equation (7) which is applicable if Knudsen number is more than 10. This value becomes 1000 at least through this simulation.  $n_1$  is the number density of iron atoms.  $\Theta$  is a dimensionless surface energy expressed by equation (8).

$$N = n_s \exp \Theta, \quad (6)$$

$$\zeta = 4 \left(\frac{3v_m}{4\pi}\right)^{1/6} \sqrt{\frac{12kT}{\rho}}, \quad (7)$$

$$\Theta = \frac{\sigma_p s_1}{kT}, \quad (8)$$

where  $n_s$  is the iron atom concentration for the saturated vapour, and  $s_1$  is the surface area of the iron atom.

#### 2.3.2. Heterogeneous condensation model of primary particle.

When the particle growth is governed by the heterogeneous condensation of the vapour, an equation for the growth rate  $G$ , which is change in diameter per unit time, expressed below can be obtained from a material balance over the growing particle and is represented by the following equation [19].

$$G = \frac{4}{d_p} \frac{R_g}{R_c} D_g (X - X_s) \left\{ \frac{1 + K_n}{1 + 1.7K_n + 1.333K_n^2} \right\}, \quad (9)$$

where  $R_g$  and  $R_c$  are the molar densities of the gas phase and the condensation phase, respectively.  $D_g$  is the diffusion coefficient defined as  $\lambda \bar{v}/3$ ,  $\lambda$  is the mean free path of iron atoms,  $\bar{v}$  is the mean speed of iron atoms [20].  $(X - X_s)$  represents the difference of gas-phase mole fraction and equilibrium state mole fraction.  $K_n$  is the Knudsen number defined as  $K_n = \lambda/(d_p/2)$ .

#### 2.3.3. Coagulation model of secondary particle.

The primary particles generated by the nucleation grow through not only the condensation of iron atoms but also the coagulation caused by collisions between particles. In this model, the coagulation process is calculated by analysing movements and collisions of particles distributed in the simulation region. A two-dimensional simulation region for the coagulation model is defined for shortening time. The size of the region is determined by the number density of primary particles obtained from the primary particle model to include 1000 particles in the region. The three-dimensional number density of primary particles determined by the primary particle model is converted into the two-dimensional number density by raising it to the 2/3rd power. Secondary particles with various shapes and sizes are formed in arc welding because the formation is very stochastic. However, only several or several tens of secondary particles are analysed as examples for the formation in this simulation due to the limitation of computational resource.

When the nucleation occurs, a primary particle is posted at a random position in the region and an initial velocity with a random direction is given to the particle. The initial velocity is determined from the thermal velocity calculated from the surrounding plasma temperature. The sum of the momenta is conserved through a particle collision. If the particles collide at a temperature above the melting point, they fuse into one spherical particle conserving their volumes. In other cases, they attach with each other like a chain depending on the temperature compared with the melting point. A particle escaping from a boundary of the region is injected from the opposite boundary with the same velocity vector.

#### 2.3.4. Calculation conditions.

As described below, the nucleation occurs around 2000 K under this calculation condition. Therefore, the initial temperature is set to be 3000 K as that in the upstream region. The temperature is decreased by 0.5 K until the room temperature of 300 K. The homogeneous nucleation model, the condensation model and the coagulation model are solved in each temperature step. It is required to provide the metal vapour pressure and the cooling rate obtained

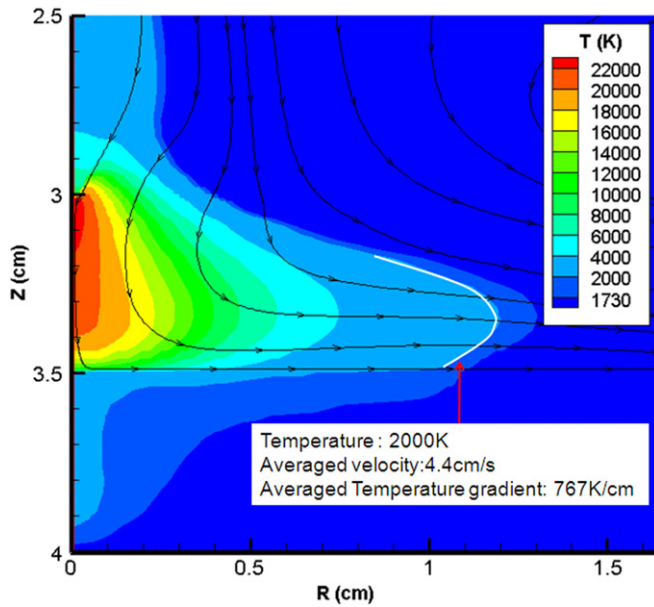


**Figure 3.** Distribution of temperature and fluid flow in helium GTA welding.

from the GTA welding model or the GMA welding model to the fume formation model as the initial conditions. The metal vapour pressure is taken from the value in the region at 3000 K. The cooling rate is calculated as the product of temperature gradient and plasma flow velocity at 2000 K. Because these values depend on positions, they should be averaged spatially in the corresponding regions.

### 3. Experimental method

In this study, stationary GTA welding was conducted for 30 s in a protective box in which helium gas was filled for avoiding oxidation of the fume in order to evaluate the reliability of the simulation model. A tungsten electrode with a conical angle of 60° and an iron base metal were employed. The arc gap was set to be 2 mm. The arc current was dc 200 A. Helium gas was introduced as the shielding gas from the torch nozzle at a flow rate of 30 L min<sup>-1</sup>. The fume was collected by a collodion thin sheet placed 4 cm above the base metal near the torch and observed with a transmission electron microscope (TEM) after the collection.

### 4. Results and discussion

#### 4.1. Fume formation mechanism in GTA welding

Figure 3 shows the distributions of temperature and streamlines of the plasma flow. The maximum temperature of the arc plasma reached 22 000 K near the cathode tip. Since the electrical conductivity of helium plasma is extremely low particularly at low temperatures, the current path is constricted within the central region where the plasma is at a high temperature [21]. Therefore, Joule heating is prompted in this region. The heat input from the arc into the base metal increases in the central region for the same reason. The weld

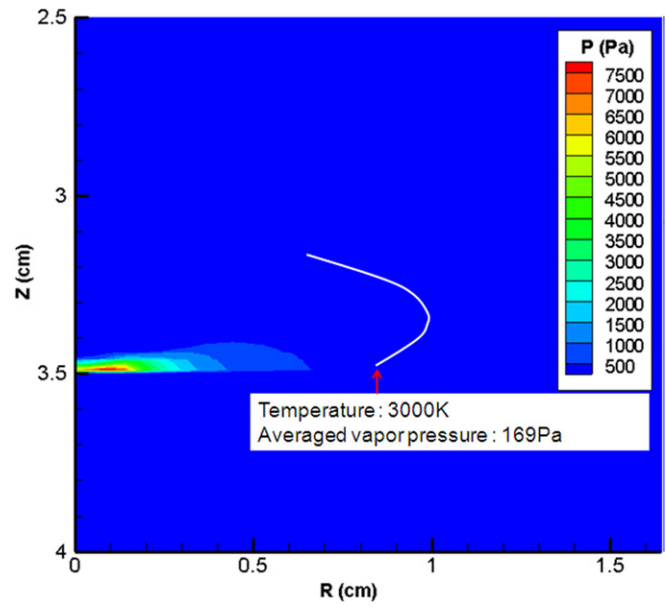


**Figure 4.** Distribution of metal vapour pressure in helium GTA welding.

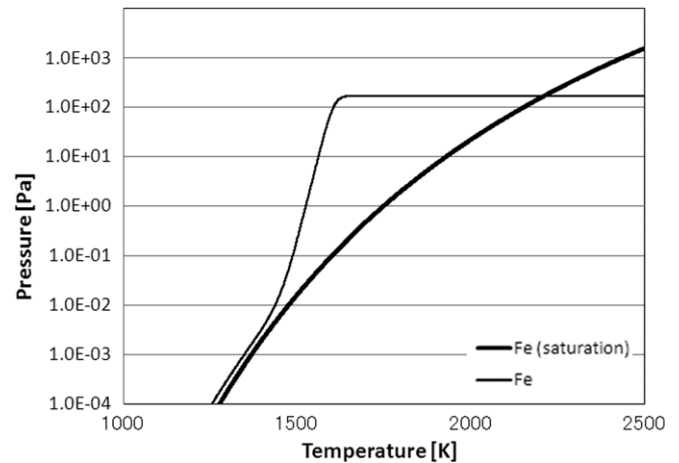
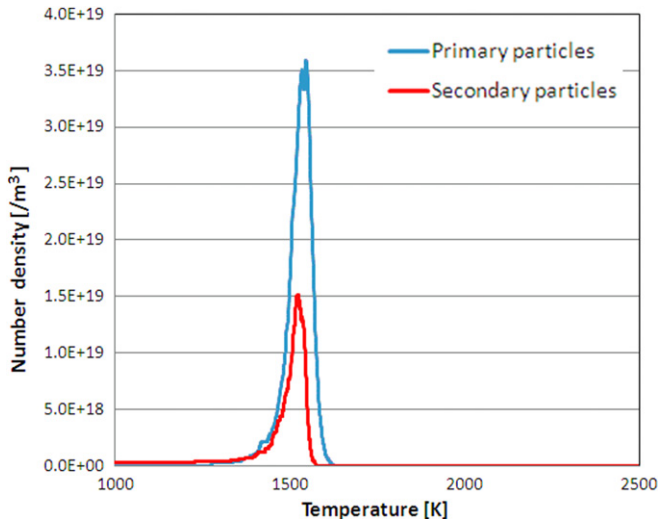


**Figure 5.** Dependence of metal vapour pressure on temperature in helium GTA welding.

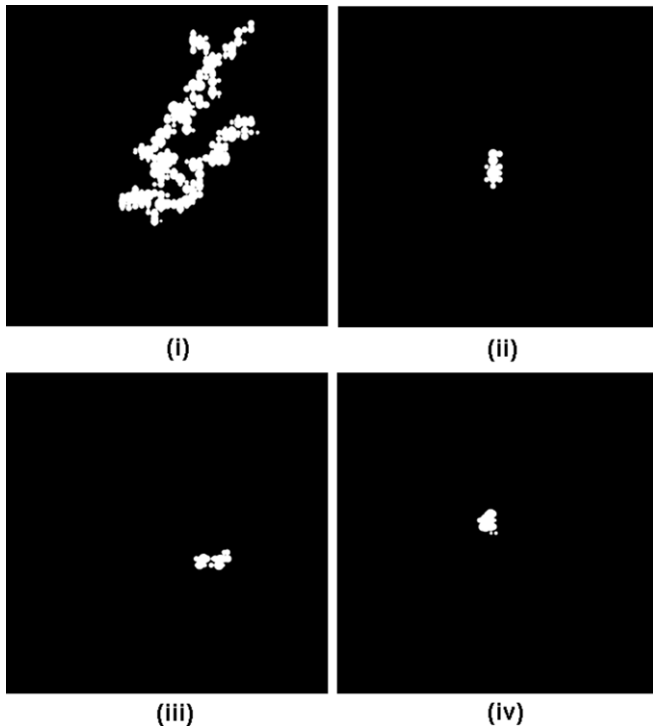
pool in the base metal is heated intensively. Consequently, the maximum temperature of the weld pool rose up to 3056 K.

Figure 4 shows the distribution of partial pressure of the metal vapour evaporated from the weld pool. It was found that the metal vapour was compressed into the region near the weld pool surface due to strong plasma flow from the cathode which was called the cathode jet and was swept away in the radial direction. The maximum metal vapour pressure became 7500 Pa near the centre of the weld pool surface. As a result, the averaged cooling rate at 2000 K and the averaged metal vapour pressure at 3000 K, denoted as white lines in figures 3 and 4, were  $3.43 \times 10^5 \text{ K s}^{-1}$  and 169 Pa, respectively.

Figure 5 shows the dependence of metal vapour pressure and saturated pressure of iron on temperature, which represents a quenching phenomenon of the metal vapour. It was seen that the metal vapour was consumed considerably at 1500 K during the rapid cooling from 3000 to 300 K because of the beginning of homogeneous nucleation and the consequent heterogeneous condensation.



**Figure 6.** Dependences of number densities of primary and secondary particles on temperature in helium GTA welding.



**Figure 7.** Shapes of secondary particles at 300 K (region size is 500 nm × 500 nm) in helium GTA welding.

The size of the simulation region of the coagulation model is  $27.9 \mu\text{m} \times 27.9 \mu\text{m}$ . At around 1600 K, the nucleation began and very small primary particles appeared in the region. The particles moved at an average velocity of  $7.7 \text{ m s}^{-1}$  at 1600 K. Subsequently, the primary particles grew up by heterogeneous condensation and a part of them formed secondary particles due to coagulation. The average velocity decreased to  $1.2 \text{ m s}^{-1}$  at 1400 K because of increase in particle weight. All the primary particles became coagulated and the averaged velocity became  $0.7 \text{ m s}^{-1}$  at 1200 K. Finally, four secondary particles were formed at 300 K.

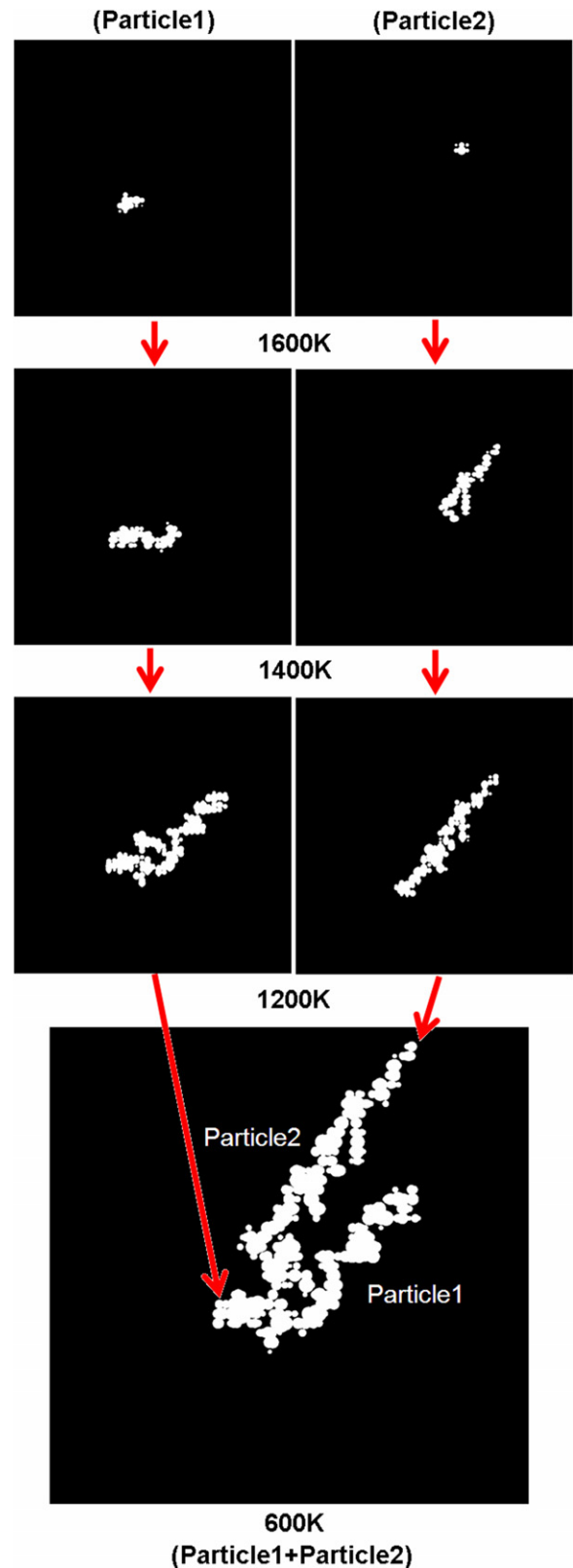


**Figure 8.** History of change in shape of a secondary particle (region size is 500 nm × 500 nm) in helium GTA welding.

Figure 6 shows the dependences of number densities of primary and secondary particles on temperature. Firstly, the number density of primary particles started to increase at around 1600 K and peaked at approximately 1500 K. After that,

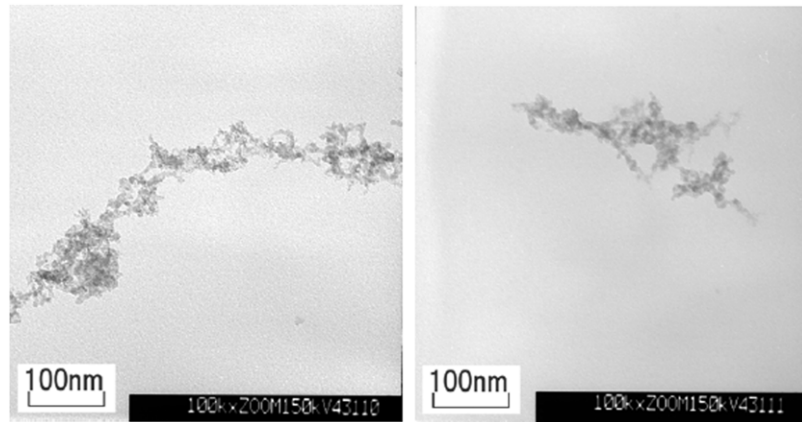


**Figure 9.** Fume shapes in helium GTA welding obtained by TEM observation.

it decreased due to the coagulation among primary particles, and that of secondary particles increased. With a further decrease in the temperature, the number density of secondary particles also decreased because of the coagulation with each other.

Figure 7 shows the magnification ( $500\text{ nm} \times 500\text{ nm}$ ) of four secondary particles (i)–(iv) formed at 300 K. It was seen that small particles of about tens of nanometres in size joined like a chain. The size of the largest particle (i) reached approximately 300 nm. Under this condition, the particles did not fuse spherically through coagulation but formed chain-like secondary particles since the nucleation occurred below the melting point of iron. Primary particles with various sizes were produced because the amount of metal vapour condensed to form primary particles changed depending on the nucleation temperature.

Figure 8 shows the coagulation process of the secondary particle (i) in figure 7 with decreasing temperature. This secondary particle (i) was formed by the collision between two large secondary particles defined as particle 1 and particle 2 at 600 K. Figure 8 also suggests that particle 1 and particle 2 grow up like a chain. This result indicates that collisions with other particles occur not on each particle surface evenly but on the edge of the secondary particle with high probability. As a reason, it is considered that the solid angle where the other particle can collide is larger at the edges of the secondary particle compared with its centre. Consequently, both particles collided with each other and the secondary particle with a U shape was formed at 600 K.

Figure 9 shows two typical shapes of the fume obtained from the TEM observation. Both secondary particles were formed by joining of primary particles like a chain. The sizes of the secondary particles reached several hundred nanometres. The small particles constituting the secondary particles were several tens of nanometres in size. These tendencies are in good agreement with simulation results.

From the above results, the fume formation mechanism in GTA welding is summarized as follows. The temperature of the arc generated between the tungsten cathode and the base metal became 22 000 K at maximum due to the thermal pinch effect. The base metal was melted by the heat input from the arc and the weld pool was formed by the convective flow caused by

driving forces such as electromagnetic force, Marangoni force, shear force and buoyancy [10]. The maximum temperature of the weld pool surface rose up to 3056 K. The maximum pressure of the metal vapour evaporated from the weld pool was 7500 Pa. The metal vapour was compressed into the region near the weld pool surface due to the cathode jet from the cathode and was swept away in the radial direction. The homogeneous nucleation occurred at around 1500 K during the outflow of the metal vapour from the arc to the surroundings of the arc. Then, very small primary particles with a size of several nanometres were produced, and the particles grew up due to the subsequent heterogeneous condensation. The secondary particles were formed through the coagulation between primary particles. Finally, the size of the secondary particles consisting of small particles with size of several tens of nanometres reached 300 nm at maximum. The secondary particle was in a U-shaped chain form.

#### 4.2. Fume formation mechanism in GMA welding

Figure 10 shows the temperature distributions at  $t = 12\text{ ms}$ ,  $14\text{ ms}$ ,  $16\text{ ms}$  and  $20\text{ ms}$  in the second cycle of metal transfer in GMA welding. It can be seen that a droplet is formed at  $t = 12\text{ ms}$ , then detached from the tip of the electrode wire at  $t = 14\text{ ms}$  and finally it is transferred to the weld pool at  $t = 20\text{ ms}$ . The droplet temperature peaked immediately before the detachment ( $t = 12\text{ ms}$ ) and became more than 3000 K near the lower surface of the droplet because the droplet was heated by electron condensation and thermal conduction from the arc covering the droplet whose temperature reached 16 000 K. There was a large temperature gradient in the droplet because the temperature near the constricted part of the electrode wire was approximately 2500 K. On the other hand, the maximum weld pool temperature was only 2400 K.

Figure 11 shows the distribution of metal vapour pressure. The metal vapour was evaporated mainly from the droplet and the tip of the wire. The metal vapour pressure became approximately 26 000 Pa at maximum near the droplet. In contrast, it was found that the metal vapour pressure near the weld pool surface was relatively low because the amount of metal vapour evaporated from the weld pool was less. This difference is caused by the higher temperature of the droplet

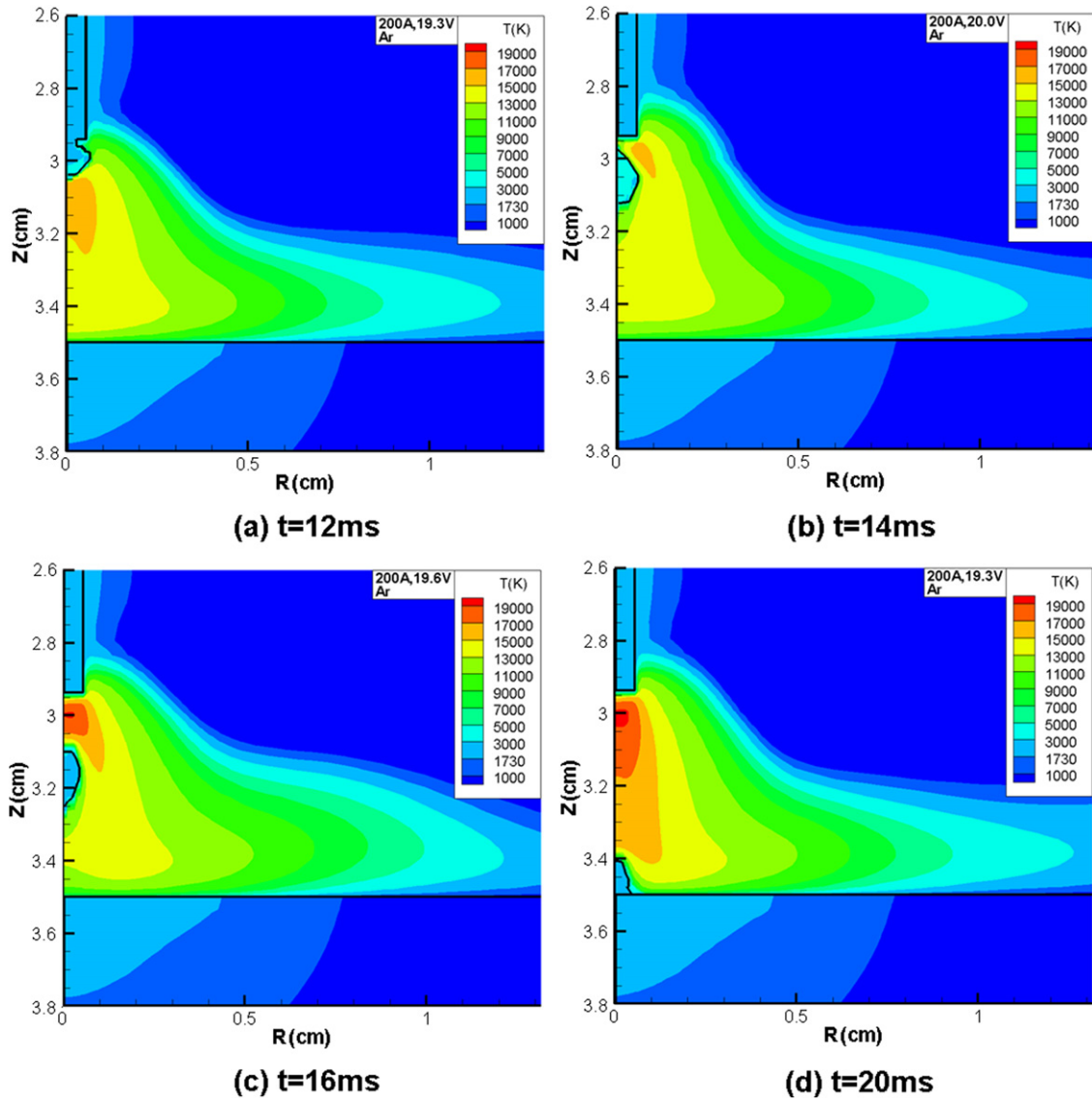


Figure 10. Time variation in temperature distribution in argon GMA welding.

compared with that of the weld pool. The metal vapour was swept away in the radial direction through the region close to the base metal surface due to the plasma flow similar to the case in GTA welding.

The metal vapour pressure and the cooling rate as initial conditions of the fume formation model were determined from the results at  $t = 12$  ms when the metal vapour pressure reached the maximum. In this study, the fume characteristics at three positions classified in the feature as shown in figures 12 and 13 were examined. At position 2, the metal vapour was swept away outwards due to the high-speed plasma flow, and therefore the metal vapour pressure was low. At position 3, the metal vapour pressure was higher than that at position 2 because of the sum of evaporation from the weld pool surface and compression due to the plasma flow from the electrode wire. Since this model assumes rotational symmetry around the arc axis, the droplet transfers along the central axis. However, in practice metal transfer tends to be unstable by various factors such as the arc pressure on the side under the droplet. Therefore, the possibility of the metal vapour near

the droplet diffusing directly to the surroundings of the arc without getting into the plasma flow should be considered. Assuming such a situation, the metal vapour pressure near the droplet and the cooling rate at the edge of the arc column adjacent to the droplet were provided in position 1. The cooling rates at positions 1, 2 and 3 were  $1.1 \times 10^5 \text{ K s}^{-1}$ ,  $5.0 \times 10^5 \text{ K s}^{-1}$  and  $1.0 \times 10^5 \text{ K s}^{-1}$ , respectively. The metal vapour pressures at each position were 26 000, 4.5 and 100 Pa.

Figure 14 shows the dependence of metal vapour pressure and saturated pressure on temperature in the same manner as figure 5. At positions 1, 2 and 3, the metal vapour was consumed at 2400 K, 1200 K and 1600 K, respectively. It was found that nucleation and condensation occurred at higher temperatures with higher metal vapour pressures provided as initial conditions.

The sizes of the regions of the coagulation model were  $210 \mu\text{m} \times 210 \mu\text{m}$ ,  $10 \mu\text{m} \times 10 \mu\text{m}$  and  $56 \mu\text{m} \times 56 \mu\text{m}$  at positions 1, 2, and 3, respectively. At position 1, a large number

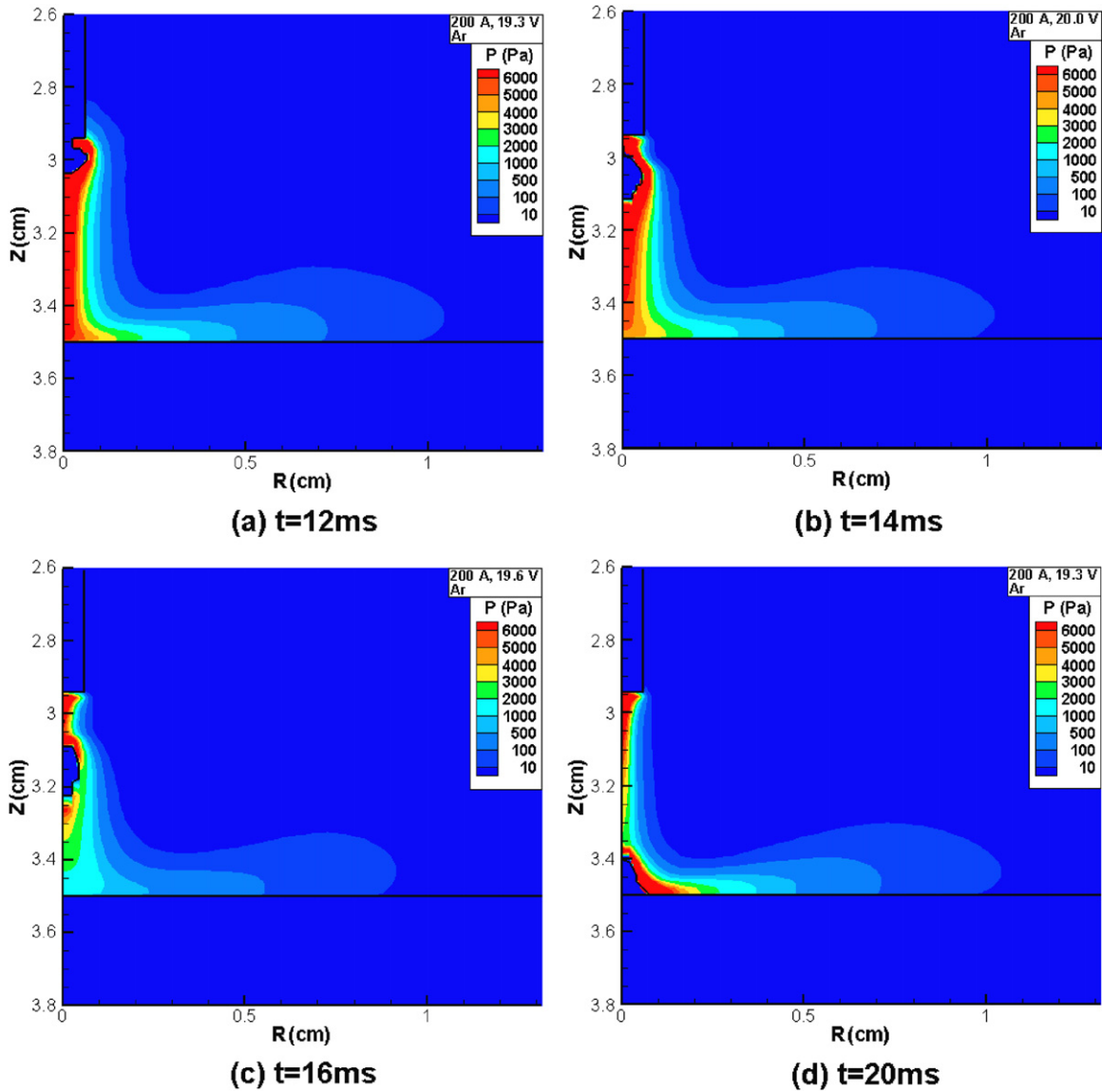


Figure 11. Time variation in metal vapour pressure distribution in argon GMA welding.

of particles existed in the region and the size of the particle reached several micrometres at maximum at 300 K. Only one secondary particle and three secondary particles were formed at positions 2 and 3, respectively.

Figure 15 shows the dependences of number densities of primary particles and secondary particles on temperature in the same manner as figure 6. At each position, the number density of primary particles began to decrease after the maximum due to the coagulation through collisions among primary particles instead of the increase in secondary particles. With a further decrease in the temperature, the number density of secondary particles also decreased because of the coagulation among them. The change in number density by coagulation was more gradual for position 1 than the other positions, and thus a high number density was maintained even at 300 K. It is considered that the collision frequency decreases because the nucleation occurs above the melting point of iron and then the size of the particle, which affects the collisional cross-section, hardly increases due to fusion in the collision.

Figure 16 shows the magnification ( $4\mu\text{m} \times 4\mu\text{m}$  for position 1,  $100\text{nm} \times 100\text{nm}$  for position 2,  $500\text{nm} \times 500\text{nm}$  for position 3) of examples of secondary particles at 300 K. Large spherical particles with sizes of several hundred nanometres were observed at position 1. It is suggested that the particle grows up due to the influence of fusion in the coagulation in addition to high metal vapour pressure near the droplet. On the other hand, at position 2 a number of primary particles with sizes of several nanometres constituted a secondary particle with a size of several tens of nanometres, because the coagulation occurred under the melting point and the metal vapour pressure was low at this position. At position 3, it can be seen that primary particles with a size of several tens of nanometres joined like a chain and constituted the secondary particle with a size of 500 nm. As a reason, it is considered that the metal vapour pressure increases near the weld pool surface because of the sum of metal vapour evaporated from the weld pool and that transported from the droplet by the plasma flow.

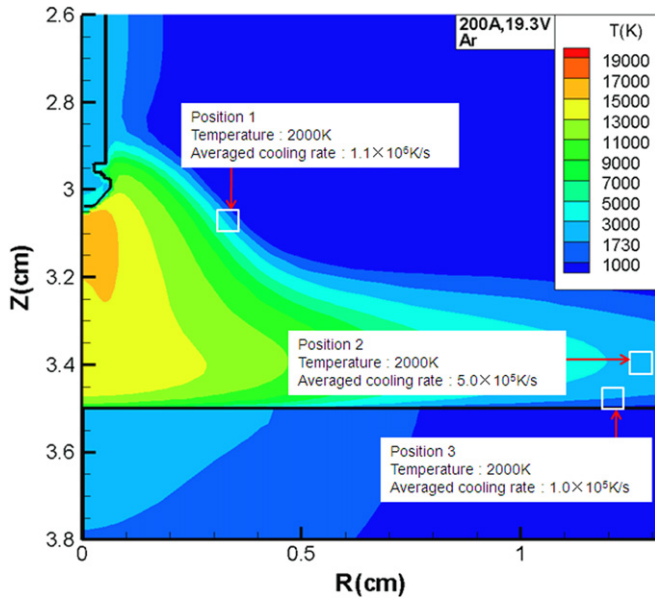


Figure 12. Distribution of temperature at  $t = 12$  ms in argon GMA welding.

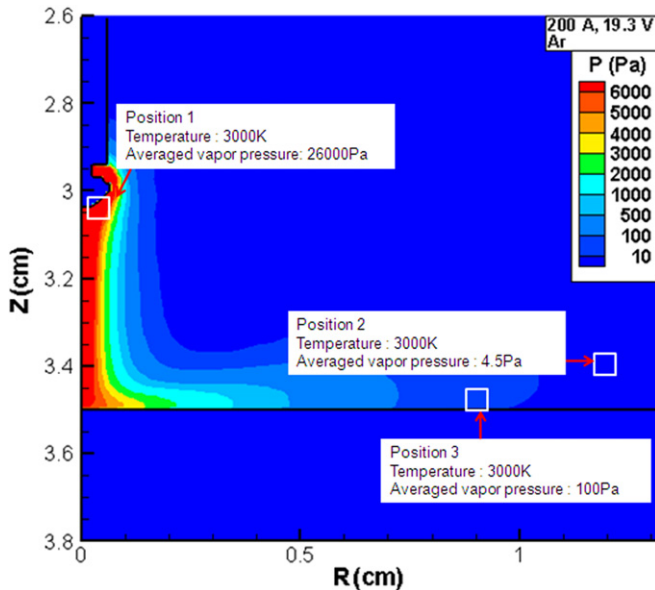


Figure 13. Distribution of metal vapour pressure at  $t = 12$  ms in argon GMA welding.

Figure 17 shows the typical experimental examples of the fume shape in GMA welding with three different types of shielding gas compositions, namely MIG (Ar + 2%O<sub>2</sub>), CO<sub>2</sub> and MAG (Ar+20%CO<sub>2</sub>). It is found that particles with the size of several tens of nanometres join like a chain and constitute a secondary particle with the size of several micrometres in MIG. In CO<sub>2</sub> and MAG, these particles grow up like a spider's web. Furthermore, a small number of large particles with a size of several hundred nanometres exist as marked in figure 17. These kinds of particles are found particularly in CO<sub>2</sub>. In the case of MIG in which the metal transfer is smooth and stable, the particle shape is similar to that at positions 2 and 3 of the simulation results as shown in figures 16(b) and (c). It is expected that a large part of the fume is produced by the

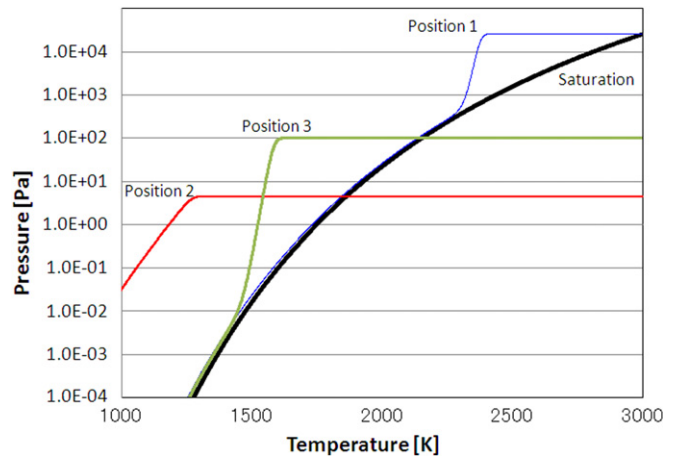


Figure 14. Dependence of metal vapour pressure on temperature in argon GMA welding.

metal vapour evaporated from the electrode wire, the droplet and the weld pool through the downstream region of the arc. In contrast, since the arc is constricted by the high specific heat of CO<sub>2</sub>, namely the *thermal pinch effect* [21], the arc pressure lifting the droplet increases in CO<sub>2</sub> and MAG welding. Consequently, the droplet tends to grow larger and the whole surface of the droplet can hardly be covered by the arc. It is suggested that the disturbance in metal transfer leads to direct diffusion and quenching of the metal vapour without a path through the downstream region of the arc. Therefore, the fume with a size of several hundred nanometres can be produced specially in CO<sub>2</sub> as shown in the simulation results at position 1 in figure 16(a).

As explained above, it was shown that most part of the fume was produced in the downstream region of the arc originating from the metal vapour evaporated mainly from the droplet by employing the GMA welding model. This kind of fume was constituted by particles with a size of several tens of nanometres and has similar characteristics to that of GTA welding. On the other hand, if the metal transfer becomes unstable and the metal vapour near the droplet diffuses directly towards the surroundings of the arc not getting into the plasma flow, the size of the particles reaches several hundred nanometres. This tendency agrees with the morphological shape of the fume in CO<sub>2</sub> and MAG obtained from experimental observations.

In this study, fume formation was assumed in inert gases such as argon and helium. However, in the future, it will be necessary to consider the influence of oxidation on fume formation, because air containing oxygen will actually exist in the surroundings of the arc. The effects of metal transfer modes, such as short arc or spray mode, on fume formation and the effect of process parameters, such as welding current, arc length, flow rate of shielding gas, on fume formation should be studied in the future because those are important for understanding the fume formation mechanism. The information obtained through this study will contribute to developing an electrode wire and to optimizing the welding conditions for reducing the fume.

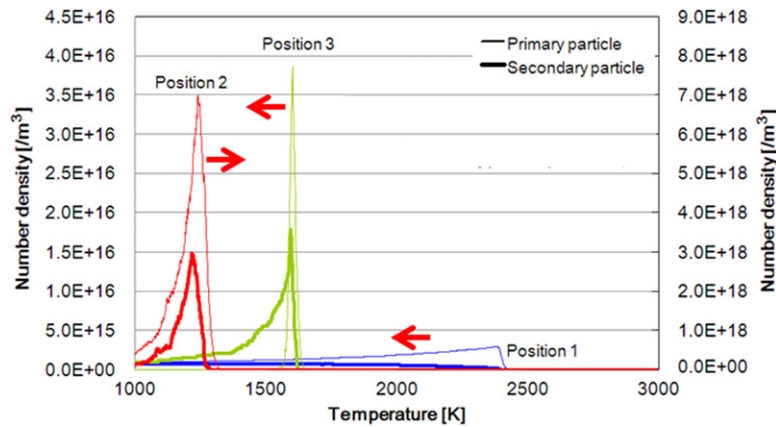


Figure 15. Dependences of number densities of primary and secondary particles on temperature in argon GMA welding.

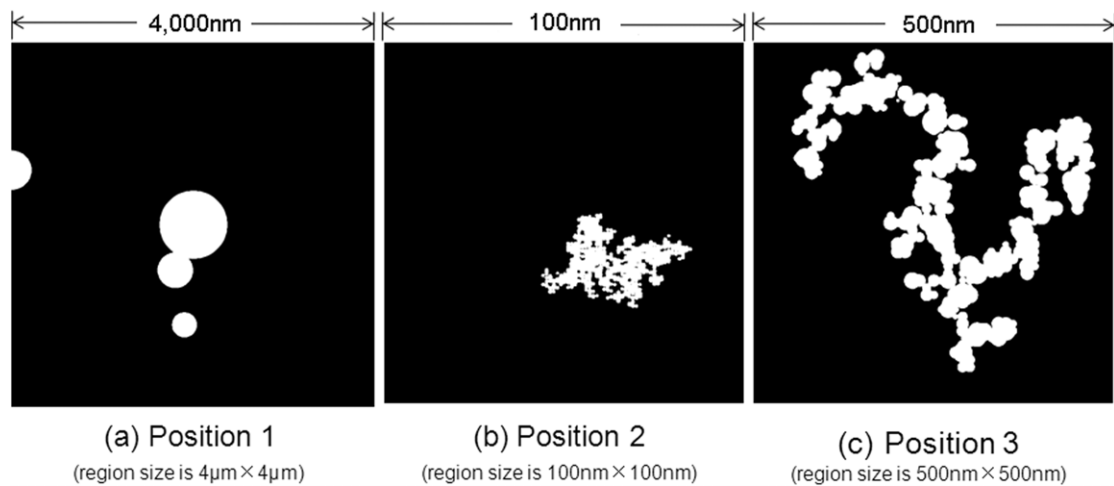


Figure 16. Shapes of secondary particles at 300 K in the case of position 1 (region size is  $4\ \mu\text{m} \times 4\ \mu\text{m}$ ), position 2 (region size is  $100\ \text{nm} \times 100\ \text{nm}$ ) and position 3 (region size is  $500\ \text{nm} \times 500\ \text{nm}$ ).

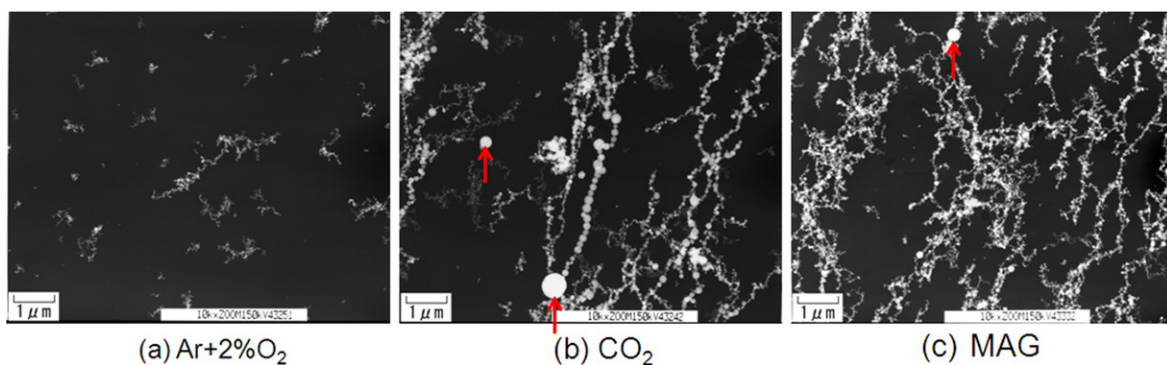


Figure 17. Fume shapes obtained by TEM observation in MIG, CO<sub>2</sub> and MAG welding.

### 5. Conclusions

The main conclusions are summarized as follows.

- (1) The averaged cooling rate and the averaged metal vapour pressure near the nucleation site in the downstream region of the arc were  $3.43 \times 10^5\ \text{K s}^{-1}$  and 169 Pa and the nucleation occurred at around 1500 K in helium GTA welding.
- (2) The size of the secondary particles consisting of small particles with a size of several tens of nanometres reached 300 nm at maximum and the secondary particle was in a U-shaped chain form in helium GTA welding.
- (3) The shape of the fume collected in helium GTA welding was experimentally observed by TEM and was in good agreement with the simulation results.
- (4) Most of the fume was produced in the downstream region of the arc originating from the metal vapour evaporated

mainly from the droplet in argon GMA welding. This kind of fume was constituted by particles with a size of several tens of nanometres and has similar characteristics to that of GTA welding.

- (5) If the metal vapour near the droplet was assumed to diffuse directly towards the surroundings of the arc not getting into the plasma flow, the size of particles reaches several hundred nanometres in GMA welding. This tendency agreed with the fume shape in CO<sub>2</sub> and MAG obtained from experimental observations.

## References

- [1] Terasaki H, Tanaka M and Ushio M 2002 *Metall. Mater. Trans. A* **33** 1183–8
- [2] Kobayashi M, Maki S, Hashimoto Y and Suga T 1980 *J. Japan Weld. Soc.* **49** 454–61
- [3] Jenkins N T and Eagar T W 2005 *Weld. J.* **84** 87-s–93-s
- [4] Bosworth M R and Deam R T 2000 *J. Phys. D: Appl. Phys.* **33** 2605–10
- [5] Watanabe T, Atsuchi N and Shigeta M 2007 *Thin Solid Films* **515** 4209–16
- [6] Schmid H J, Al-Zaitone B, Artelt C and Peukert W 2006 *Chem. Eng. Sci.* **61** 293–305
- [7] Tanaka M and Lowke J J 2007 *J. Phys. D: Appl. Phys.* **40** R1–R23
- [8] Yamamoto K, Tanaka M, Tashiro S, Nakata K, Yamazaki K, Yamamoto E, Suzuki K and Murphy A B 2009 *Q. J. Japan Weld. Soc.* **27** 4s-7s
- [9] Mori Y, Iwao T, Yumoto M, Tashiro S and Tanaka M 2009 *Q. J. Japan Weld. Soc.* **27** 8s-12s
- [10] Yamamoto K, Tanaka M, Tashiro S, Nakata K, Yamazaki K, Yamamoto E, Suzuki K and Murphy A B 2008 *Sci. Technol. Weld. Join.* **13** 566–72
- [11] Menart J and Lin L 1999 *Plasma Chem. Plasma Process.* **19** 153–70
- [12] Wilke C R 1950 *J. Chem. Phys.* **18** 517–9
- [13] Murphy A B 1996 *J. Phys. D: Appl. Phys.* **29** 1922–32
- [14] The Japan Institute of Metals 1993 *Data Book of Metals* 3rd edn (Tokyo: Maruzen Co., Ltd) (in Japanese)
- [15] Murphy A B 1995 *Plasma Chem. Plasma Process.* **15** 279–307
- [16] Patanker S V 1980 *Numerical Heat Transfer and Fluid Flow* (New York: Hemisphere)
- [17] Friendlander S K 1983 *Ann. New York Acad. Sci.* **404** 354–64
- [18] Girshick S L, Chiu C P and McMurry P H 1990 Time-dependent aerosol models and homogeneous nucleation rate *Aerosol Sci. Technol.* **13** 465–77
- [19] Joshi S V, Liang Q, Park J Y and Batdorf J A 1990 *Plasma Chem. Plasma Process.* **10** 339–58
- [20] Fuchs N A and Sutugin 1971 *Topics in Current Aerosol Research (International Reviews in Aerosol Physics and Chemistry vol 2)* (Oxford: Pergamon)
- [21] Murphy A B, Tanaka M, Yamamoto K, Tashiro S, Sato T and Lowke J J 2009 *J. Phys. D: Appl. Phys.* **42** 194006